Accepted manuscript doi:
10.1680/jencm.18.00018

Accepted manuscript doi:
10.1680/jencm.18.00018

Submitted: 29 March 2018

Published online in 'accepted manuscript' format: 08 October 2018

Manuscript title: Numerical analysis of fluid-rock interactions in hydraulic fracturing

Authors: Davood Mahdavian and Akbar Javadi

Affiliation: University of Exeter, Exeter, UK

Corresponding author: Davood Mahdavian, University of Exeter, Exeter, UK. Tel.: 07463605246.

E-mail: dm464@exeter.ac.uk

Accepted manuscript doi:
10.1680/jencm.18.00018

Abstract

Hydraulic fracturing is a process of fluid injection into the well. This process creates tensile stresses in the rock in order to overcome the tensile strength of the formation. In this study, a three-phase hydro-mechanical model is developed for simulating hydraulic fracturing. The three phases include: porous solid, fracturing fluid and reservoir fluid. Two numerical simulators (ANSYS Fluent for fluid flow and ANSYS Mechanical for geomechanical analysis) are coupled together to model multiphase fluid flow in hydraulically fractured rock undergoing deformations, ranging from linear elastic to large, nonlinear inelastic deformations. The two solvers are coupled, using system coupling in ANSYS Workbench. The coupled problem of fluid flow and fracture propagation is solved numerically. The fluid flow model involves solving the Navier-Stokes equations using the finite volume method. The flow model is coupled with the geomechanics model to simulate the interaction between fluid flow inside the fracture with rock deformations. For any time step, the pore pressures from the flow model are used as input for the geomechanics model for the determination of stresses, strains, and displacements. The strains derived from the gomechanics model are in turn used to calculate changes to the reservoir parameters that are fed as input to the flow model. This iterative process continues until both (fluid and solid) models are converged. A parametric study is conducted by changing various model parameters to study their effects on the hydraulic fracturing process. The results show that changes in rock mechanical properties as well as fluid parameters could lead to significant changes in the hydraulic fracture propagation.

Keywords: Rock Mechanics; Fluid Mechanics; Energy; Failure; Coupling

Accepted manuscript doi:
10.1680/jencm.18.00018

1-Introduction

The technology of hydraulic fracturing has been widely used for reservoir stimulation, especially for unconventional reservoirs (Economides and Nolte, 2000). Coupled rock deformation and fluid flow in fractured porous media is important for reservoir simulation because rock deformation exerts an important influence on reservoir production.
Optimal design of hydraulic fracturing is a fundamental problem in Petroleum Engineering and plays a critical role in many applications within the oil and natural gas industry. The process of hydraulic fracturing can be generally defined as initiation and propagation of fractures due to the pressurization of fluid flow within existing fractures. Hydraulic fracturing involves the interaction between four different phenomena:
(1) Porous medium deformation;
(2) Pore fluid flow;
(3) Fracturing fluid flow; and
(4) Fracture propagation.
The equations and constitutive relations governing these coupled processes are Biot's theory of poroelasticity for porous media, Darcy's law for pore fluid flow, Reynold's lubrication theory for fracturing fluid flow and the cohesive zone model to characterize fracturing. The focus of this study is the effect of fluid flow and formation properties on hydraulic fracturing process.

The interaction between fluid and solid processes, commonly known as coupling, arises in geological media due to the presence of deformable, fluid-filled pores and discontinuities. Depending on the type of processes involved, the hydromechanical (HM) response of a rock mass can be fully reversible if associated with elastic deformations only, or irreversible if associated with processes such as yielding, fracturing, and frictional slipping along discontinuities. Advances in theoretical and numerical modelling in coupled HM processes have been driven by several geomechanical applications, including:

Rock engineering: e.g., landslides and slope instabilities, dam foundation failures, and stability of underground and surface excavations;
Nuclear waste management: e.g., design and performance assessment of underground nuclear waste repositories;
Oil and gas exploration and production: e.g., borehole stability, reservoir compaction and subsidence, and hydraulic fracturing and stimulation;
Geothermal energy extraction: e.g., enhanced geothermal systems;
Mining: e.g., coal mining and coal methane extraction; and
Storage of fluid underground: e.g., carbon sequestration, geological storage of natural gas, and liquid waste disposal (Mahabadi, 2012).
The interaction between fluid and structure occurs in a system where flow of a fluid causes a solid structure to deform which, in turn, changes the boundary condition of the fluid system. This can also happen the other way around where the structure makes the fluid flow properties to change. This kind of interaction occurs in many natural phenomena and man-made engineering systems. It becomes a crucial consideration in the design and analysis of different engineering systems. Fluid-structure interaction simulations are also conducted to avoid flutter on aircraft and turbo-machines (Yun and Hui, 2011).

In this study, the development of an incremental approach to evaluate the hydraulic fracturing is investigated in a shale reservoir. A numerical method is developed to simulate the hydro-

mechanical evolution of the fracture and of the surrounding rock in the finite element analysis framework. The propagation and the exchanges of fluid with the low permeable porous medium are considered. The ability of cohesive elements to model fluid-driven crack propagation in the viscosity-dominated regime is investigated. Hydraulic fractures for reservoir stimulation typically propagate in the viscosity-dominated regime. In this study, we focus on the governing equations of the coupled problem: lubrication equation, pressure continuity and cohesive zone model.

2-Hydraulic fracturing models

The first simplified theoretical models for hydraulic fracturing were developed in the 1950s (Crittendon 1950, Harrison et al. 1954 and Hubbert and Willis 1957). One of the most important papers that were published in this area was by Perkins and Kern who adapted the classic Sneddon plane strain crack solution to develop the so-called PK model (Figure 1). Later, Nordgren adapted the PK model to formulate the PKN model, which included the effects of fluid loss. Khristianovic and Zheltov, and Geertsma and de Klerk independently developed the so-called KGD (plane strain) model (Figure 2). The radial or penny-shaped model (Figure 3) with constant fluid pressure was solved by Sneddon. The problem of a flat elliptical crack under constant loading was studied by Green and Sneddon (Adachi et al, 2007).

The PKN and KGD models differ in one major assumption: the way in which they convert a three-dimensional solid and fracture mechanics problem to a two-dimensional plane strain model. Khristianovic and Zheltov assumed plane strain in the horizontal direction i.e. all horizontal cross sections act independently or equivalently, which is equivalent to assuming that the fracture width changes much more slowly vertically along the fracture surface from any point on the fracture surface than it does horizontally. In practice it is true if the fracture height is much greater than the length or if free slip occurs at the boundaries of pay zone. Perkins and Kern, on the other hand, assumed that each vertical cross section acts independently (Figure 1), which is equivalent to assuming that the pressure at any section is dominated by the height of the section rather than the length of the fracture. This is true if the length is much greater than the height. This difference in one basic assumption has lead to two different ways of solving the problem. In the case of the PKN model, the effect of the fracture tip is not considered; the concentration is on the effect of fluid flow and the corresponding pressure gradients. In the KGD model, however, the tip region plays a much more important role (Dahi, 2009).

3-Computational analysis

The analysis of hydraulic fracturing has gained a wide interest in the petroleum engineering community. As the importance of hydraulic fracturing treatment rapidly increases, some modelling tools have been developed to estimate the progressive failure phenomenon in unconventional reservoirs. The finite element method (FEM) is the most widely used numerical tool in fracture mechanics. Several improvements, such as singularity or interface elements have been suggested to improve the linear elastic fracture mechanics modelling in the FEM. In the FEM, individual elements are connected together by a topological mapping, and local polynomial representation is used for the fields within the element. The solution obtained is a function of the quality of mesh, and the mesh has to conform to the geometry. Therefore, the displacements near fracture tip have to be captured by refining the mesh

Accepted manuscript doi:
10.1680/jencm.18.00018

locally (Chan et al,1975).

The finite element method is an efficient way to calculate the stress intensity factor due to the complexity of the geometry and boundary conditions. In this study the finite element software ANSYS is used to simulate the hydraulic fracturing process. In ANSYS, there are 3 main ways to evaluate fracture mechanics parameters:

- Stress intensity factors (K)
- J-integral JINT (J)
- Energy release rate VCCT (G)

3.1-Stress Intensity Factors (SIF)

Crack propagation analysis requires the evaluation of the parameters such as the energy release rate and stress intensity factors (SIF) to determine the length, velocity and orientation of the crack propagation. The stress intensity factor is used in fracture mechanics to accurately predict the stress state near the tip of a crack caused by loads. The stress intensity factor is the magnitude of stress singularity at the crack tip (Anderson 1994).
The stress-intensity factor, K, is a parameter to characterize the stress field ahead of a sharp crack in a test specimen or a structural member. The parameter, K, is related to the nominal stress level (σ) in the structural member and the size of the crack, and has the unit of ($MPa.mm^{0.5}$). In general, the relationship is represented by:

$$K = \sigma\sqrt{a}p \qquad (1)$$

where p is a geometrical parameter that depends on the structural member and crack size, a is the crack length. All structural members or test samples that have flaws can be loaded to different levels of K. This is similar to the situation where unflawed structural can be loaded to different levels of stress (σ) (Barsom and Rolfe, 1999).
The magnitude of stress intensity factor depends on sample geometry, the size and location of the crack, and the magnitude and the modal distribution of loads on the material. The energy release rate for crack growth or strain energy release rate is the change in elastic strain energy per unit area of crack growth. The well-known criteria for crack propagation are maximum circumferential (hoop) stress (Erdogan and Sih 1963), maximum energy release rate (Nuismer 1975), and maximum strain energy density criterion (Sih 1974).

3.2-J-integral JINT (J)

The J-Integral evaluation is based on the domain integral method proposed by Shih. The domain integration formulation applies area integration for 2-D problems and volume integration for 3-D problems. Area and volume integrals offer much better accuracy than contour integral and surface integrals, and are easier to implement numerically (Shih and et al, 1986).

3.3-Energy release rate VCCT (G)

Energy release rate is based on the assumption that the energy needed to separate a surface is the same as the energy needed to close the same surface. The approach for evaluating the energy-release rate is based on the virtual crack-closure technique (VCCT) (Delorenzi, 1982).

Accepted manuscript doi:
10.1680/jencm.18.00018

4-Mechanics of fluid flow in the fracture

The major fluid flow parameters are the fluid viscosity μ and injection rate q_i. Consider a Newtonian fluid flowing laterally through a narrow slit (Figure 4). In the case of laminar flow (the general case for flow inside hydraulic fractures), the pressure drop along some length Δx of the slit is:

$$\frac{\Delta p_{net}}{\Delta x} = \frac{12\mu q}{h_f w^3} \qquad (2)$$

where h_f is fracture height, Δp_{net} is pressure drop and w is fracture width$\bar{w}$.
The fracture is essentially a channel of varying width over its length and height. The local pressure gradient within the fracture is determined by the fracturing fluid rheology, fluid velocity and fracture width. Equations governing fluid flow within the fracture can be derived using the principle of conservation of momentum and lubrication theory applied to a fluid travelling in a narrow conduit. The rheology of fracturing fluids is generally represented by a power law model that incorporates two parameters K and n. In recognition that fluid flow within a fracture is laminar for most fracturing applications (Perkins and Kern, 1961), the global pressure gradient along the length of a fracture can be expressed as:

$$\frac{dp}{dx} \propto \frac{K v_x^n}{\bar{w}^{1+n}} \qquad (3)$$

where v_x is the average fluid velocity along the length of the fracture and is defined in terms of the volumetric injection rate q_i, fracture height h_f and height-averaged fracture width $\bar{w}$. Material balance or conservation of mass suggests that v_x is proportional to $qi/\bar{w}h_f$. Equation 3 then becomes

$$\frac{dp}{dx} \propto \frac{K}{\bar{w}^{1+2n}} \left(\frac{q_i}{h_f}\right)^n \qquad (4)$$

In the special case of a Newtonian fluid (n = 1 and K = μ, where μ is the fracturing fluid viscosity), equation 4 reduces to

$$\frac{dp}{dx} \propto \frac{\mu}{\bar{w}^2} \left(\frac{q_i}{\bar{w} h_f}\right) \qquad (5)$$

where the term $\bar{w}\, h_f$ is readily recognized as the average fracture cross-sectional area. Equation 5 is essentially Darcy's law with the permeability proportional to $\bar{w}^2$. Equations 3 and 4 are formulated in terms of the average velocity and implicitly ignore change in the fracture width over its height. The varying width profile has an effect on the flow resistance relative to the case of a constant-width channel. The increase in the flow resistance is accentuated during periods of fracture height growth into barriers at higher stress. The varying width profile affects other physical phenomena that are highly sensitive to the velocity (Economides, 2000).

Accepted manuscript doi:
10.1680/jencm.18.00018

5-Numerical Tools

5.1-Finite Element Method

Discretizing the equivalent model with finite elements as shown in Figure 5, we can achieve a finite element equation for the solid medium as

$$\mathbf{K}_u\mathbf{U} = \mathbf{F} \tag{6}$$

where K_u is the global stiffness of the solid elements, U is the global nodal displacement, and F is the equivalent global nodal force of the net pressure.

As only net pressure has contribution to F, equation (6) can be rewritten as

$$\mathbf{K}_u\boldsymbol{U} - \boldsymbol{BP} = 0 \tag{7}$$

where **P** is a vector of nodal net pressure, and matrix **B** transfers the net pressures into equivalent nodal forces. The conservation of the incompressible fluid in the fracture leads to its weak form as

$$\int_{\gamma}\left[-\nabla(dp).q + (dp)\frac{\partial w}{\partial t} + (\partial p)g\right]dl + dpq \mid s = 0 \tag{8}$$

where δ_p is any allowable testing function, and S is the collection of boundary conditions of flow. Therefore, a finite element equation for fluid flow within the fracture is cast as

$$\mathbf{K}_w(\mathbf{W})P + \mathbf{LW} + \mathbf{H} = 0 \tag{9}$$

where **W** is a vector formed by the widths of the nodes on the fracture surface, $\mathbf{K}_w$ is the assembly of the flux stiffness of the fluid elements and is a function of **W**, **L** is the assembly of the length stiffness of the fluid elements, and **H** concludes the contributions of the fluid leak-off and the fluid injection (Devloo et al, 2006).

Taking time integration with equation (9), we have

$$\int_{tn}^{tn+1}[\,\mathbf{K}_w\,(\mathbf{W})P + \mathbf{LW} + \mathbf{H}]dt = 0 \tag{10}$$

The backward Euler scheme for time difference is used in this paper. So according to equation (10) we have

$$\mathbf{K}_w(\mathbf{W}_{n+1})\mathbf{P}_{n+1}\Delta t - \mathbf{L}(\mathbf{W}_{n+1} - \mathbf{W}_n) + \mathbf{H}\Delta_t = 0 \tag{11}$$

where $\mathbf{W}_{n+1}$ and $\mathbf{P}_{n+1}$ are the unknown fracture width and net fluid pressure at the (n + 1)-th step, respectively, $\mathbf{W}_n$ is the known fracture width at the n-th step, and Δt is the time step between the n-th step and the (n + 1)-th step.

Equation (11) can be rewritten in an alternative way as

Accepted manuscript doi:
10.1680/jencm.18.00018

$$\mathbf{K}_{\mathrm{w}}(\mathbf{U}_{\mathrm{n+1}})\mathbf{P}_{\mathrm{n+1}}\Delta_t + \acute{\mathbf{L}}\left(\mathbf{U}^{\mathrm{f}}_{\mathrm{n+1}} - \mathbf{U}^{\mathrm{f}}_{\mathrm{n}}\right) + \mathbf{H}\Delta t = 0 \qquad (12)$$

where $\mathbf{U}^{\mathrm{f}}_{\mathrm{n+1}}$ and $\mathbf{U}^{\mathrm{f}}_{\mathrm{n}}$ are the displacements of the nodes on the fracture surface at the (n + 1)-th step and n-th step, respectively, and $\acute{\mathbf{L}}$ determines the contribution of nodal displacements on the fracture surface to fracture widths. Note that $\mathbf{U}^{\mathrm{f}}_{\mathrm{n+1}}$ is a subset of $\mathbf{U}_{\mathrm{n+1}}$, and $\mathbf{U}^{\mathrm{f}}_{\mathrm{n}}$ is known a priori.

In every step, Equation (11) leads to a new equation written as

$$\boldsymbol{K}_u\boldsymbol{U}_{n+1} - \boldsymbol{B}\boldsymbol{p}_{n+1} = 0 \qquad (13)$$

$\mathbf{U_{n+1}}$ and $\mathbf{P_{n+1}}$ can be obtained by solving the coupled equations (12) and (13) (Bao et al, 2014).

5.2-Computational Fluid Dynamics

The Computational Fluid Dynamics (CFD) code, FLUENT, was used for numerical analysis of fluid flow. The code uses a finite volume-based technique to convert the governing mathematical equations to algebraic equations that can be solved numerically. The code is supplemented by a proprietary ANSYS based geometry construction and meshing engine, which allows users to build and mesh complex flow models to be used by the solver (Versteeg and Malalasekara, 1995).

Like most CFD programs, Fluent is based on the finite volume method (FVM). The finite volume method is a generalization of the finite difference method to unstructured meshes. Unlike the finite element method, FVM yields values across the entire volume contained within a cell. This has a particular advantage in preserving the flux of state variables across intercellular surfaces (Wilkes, 1999).

We are interested in using CFD to solve the Navier–Stokes equations or some coherent simplified subset of these. These are the set of equations which, taken together, completely describe continuum hydrodynamics. The momentum conservation equations are:

$$\rho\left(\frac{\partial u}{\partial t} + u\frac{\partial u}{\partial x} + v\frac{\partial u}{\partial y} + w\frac{\partial u}{\partial z}\right) = \frac{\partial p}{\partial x} + \mu\left(\frac{\partial^2 u}{\partial x^2} + \frac{\partial^2 u}{\partial y^2} + \frac{\partial^2 u}{\partial z^2}\right)$$

$$\rho\left(\frac{\partial v}{\partial t} + u\frac{\partial v}{\partial x} + v\frac{\partial v}{\partial y} + w\frac{\partial v}{\partial z}\right) = \frac{\partial p}{\partial y} + \mu\left(\frac{\partial^2 v}{\partial x^2} + \frac{\partial^2 v}{\partial y^2} + \frac{\partial^2 v}{\partial z^2}\right)$$

$$\rho\left(\frac{\partial w}{\partial t} + u\frac{\partial w}{\partial x} + v\frac{\partial w}{\partial y} + w\frac{\partial w}{\partial z}\right) = \frac{\partial p}{\partial z} + \mu\left(\frac{\partial^2 w}{\partial x^2} + \frac{\partial^2 w}{\partial y^2} + \frac{\partial^2 w}{\partial z^2}\right) \qquad (14)$$

The associated continuity equation is

$$\frac{\partial u}{\partial x} + \frac{\partial v}{\partial y} + \frac{\partial w}{\partial z} = 0 \qquad (15)$$

where, *u*, *v*, *w* are *x*, *y*, *z* components of velocity respectively. The continuity equation (equation 15), and the Navier-Stokes equations (equation 14) completely describe the motion of an incompressible fluid in a continuum medium in 3D (Wilkes, 1999).

Accepted manuscript doi:
10.1680/jencm.18.00018

Broadly, the strategy of CFD is to replace the continuous problem domain with a discrete domain using a grid. In the continuous domain, each flow variable is defined at every point in the domain. Appropriate initial and boundary conditions need to be applied in order to solve the Navier-Stokes equations and continuity equations. The boundary conditions in a 2D crack on the wall of a production well, which are used in this study, are as follows:

- No-slip boundary condition is used to bound fluid and solid regions.
- Velocity inlet boundary conditions are used to define the velocity and scalar properties of the flow at inlet boundaries.
- Pressure inlet boundary conditions are used to define the total pressure and other scalar quantities at flow inlets.
- Pressure outlet boundary conditions are used to define the static pressure at flow outlets.

In addition, material properties including density and viscosity for each zone are specified. It is important to accurately represent a boundary layer or fully developed turbulent flow at the inlet but in this study laminar flow is used. Multiple upstream meshes can be used in Fluent, giving users the flexibility to select the most efficient mesh combinations for different applications but Tetrahedral mesh, is used in this study.

The advantage of using tetrahedral mesh is that it gives an indication of how the mesh is likely to respond to the deformations experienced during simulation. This is in contrast to many traditional methods that may produce an initial mesh with good quality measures, but also with hidden deficiencies that can be revealed during simulation leading to poor accuracy or element collapse.

6-Coupling

Multi-physics problems are very difficult to solve by analytical methods and using numerical or experimental methods is the best way to solve them. Advanced techniques and the availability of powerful commercial software tools in both fluid and solid parts have made this numerical simulation possible. There are three different coupling methods for solving coupled problems: full coupling, loose coupling and one-way coupling

6.1-One-way Coupling

In one-way coupling, two separate sets of equations are solved independently over the same total time interval. Periodically, output from one simulator is passed as input to the other; however, information is passed in only one direction. For example, pore pressures might be sent from the flow code to the mechanical simulation code as input load to calculate the mechanical responses such as stresses, strains, and displacements. No information would be passed back from mechanical model to flow model, however. In most practical applications, the two simulators are in fact run independently. One can often gain valuable insight into the physical situation from one-way coupling, and it is clearly preferable to fluid flow alone (Fredrich et al., 1996, 1998).

Accepted manuscript doi:
10.1680/jencm.18.00018

6.2-Two-way coupling

This type of coupling is applied to problems where the motion of a fluid influences a solid structure and at the same time the flow of fluid is influenced by reaction of the solid structure. During the first time step, converged solutions of the fluid calculation provide the forces acting on the solid body. Then the forces are interpolated to the structural mesh like in one-way coupling and the solution from the structural solver is obtained with those fluid forces as boundary conditions. As a consequence, the mesh is deformed according to the response of structure. These displacement values are interpolated to the fluid mesh, which results in deformation of the fluid domain. This process is repeated until both force and displacement values are converged below the pre-determined limit (Benra et al, 2011).

6.3-Full Coupling

To develop a fully coupled simulator, a single set of equations incorporating all of the relevant physics must be solved simultaneously. As an example, the traditional porous flow equations for a rigid matrix would be modified to include terms for mechanical deformation. Full coupling is often the preferred method for simulating multi-physics problems since it should theoretically produce the most realistic results. Unfortunately, deriving a fully coupled multiphase flow simulator that models nonlinear, inelastic mechanical deformations is extremely difficult. Thus with fully coupled models, often the mechanical part is simplified by the assumption of linear elasticity (Lewis and Sukirman, 1993a,b; Lewis and Ghafouri, 1997; Osorio et al., 1999).

The present study describes a loose coupling approach, which is somewhere between full and one-way coupling. In loose coupling, there are two sets of equations, which are solved independently, but information is passed at designated time intervals in both directions between the two simulators. Laminar flow was used in this study. The existing crack length and width were 200 mm. The borehole diameter and length were 30 cm and 200 cm respectively and it was drilled in a shale formation. Figure 6 shows the horizontal borehole and the fracture inside a shale reservoir.

Workbench can be used to perform coupled simulations using two or more systems (ANSYS Mechanical and ANSYS Fluent in this case) using a System Coupling component. One-way or two-way fluid-structure interaction analysis can be set up in Workbench by connecting a System Coupling component to the Mechanical system and to the ANSYS Fluent fluid flow analysis system.

The fluid pressure at the start of pumping was 9 MPa and fluid velocity was 5 m/s. Young’s modulus, Poisson’s ratio and fluid viscosity were respectively 25 GPa, 0.2 and 0.0003 pa.s. Figure 8 shows the hydraulic fracture after pumping high-pressure fluid and coupling of two solvers.

Accepted manuscript doi:
10.1680/jencm.18.00018

7-Numerical Results

Rock mechanical properties such as Young's modulus, and Poisson's ratio have significant influences on hydraulic fracturing operation. It is important to note that, these parameters are uncontrollable and are totally dependent to the rock formation properties, which arise from geological conditions. Meantime, other parameters such as fluid viscosity and leak-off coefficients play important roles in designing a hydraulic fracturing fluid, which can simply change the hydraulic fracturing opening. By knowing the influences of the above parameters on opening of cracks, the capability of proppant transport and the probability of bridging and eventually any job failure can be somehow predicted.

Figure 9 shows the variation of stress intensity factor as a function of the crack length along the cohesive elements in reservoir domain. Despite complex loading conditions and various loads in hydraulic fracturing, stress intensity field in the crack tips, created from any source of loading, can be formulated using the principle of superimposition of stress intensity factors.

J-integral is a parameter that can be used for crack propagation analysis. Figure 10 shows the variation of J-Integral with crack length. It is seen that J-Integral increases with increasing the crack length. This can be attributed to the concept that with a growth in crack length, component of released elastic energy in J-Integral ascends. The figure shows, that in the first stage, the rate of variation of J-integral has a descending trend and after reaching a minimum value, the trend changes the course and adopts an ascending approach.

The reason for this phenomenon can be explained by the fact that in the first stages, the released energy is consumed to propagate and develop the cracks and to overcome the surface crack energy. Minimum value of J-integral in this figure shows that the crack has reached its final propagation phase and after which, by increasing fluid injection, the crack does not propagate and causes an increase in elastic strain energy in the rock that makes the potential energy grow up.

Figure 11 shows the variation of critical pressure of crack propagation with changes in crack length growth at different pressures. As can be seen, by increasing the crack length, the critical crack propagation pressure decreases. It shows that the bottom hole pressure drops with time while the fracture length increases. This result is a consequence of assuming an infinite height for the fracture (KGD geometry), which indicates that longer fractures require less pressure to maintain the same opening.

In general, increasing the fracturing fluid viscosity in injection operation can considerably increase the fracture stress intensity factor. Based on Figure 12, as viscosity increases from 0.3 to 0.9 Pa.s, a meaningful increase in stress intensity factor that can be easily observed. The higher fluid viscosity leads to increasing net wellbore pressure that acts on the fracture surface area, which results in further opening of the fracture.

Figure 13 shows the effect of Young's modulus on crack propagation. The results show that, by increasing elastic modulus from 25 to 50 GPa, the stress intensity factor has steeply increased from 0.25 to 1.2 MPa.√mm. It can be concluded that rocks with higher elastic modulus can be fractured easier.

Accepted manuscript doi:
10.1680/jencm.18.00018

Poisson's ratio indicates how much a rock that is shortened in one direction expands in the other two directions. The results show that increasing Poisson's ratio from 0.2 to 0.5, increases the stress intensity factor from 0.5 to 1.7 MPa.√mm (Figure 14). So, based on the definition of Poisson's ratio, it can be concluded that any increase in this parameter would affect the local stresses as well as the extent of strain level and deformation near the crack tip, which can significantly increase the crack propagation.

8-Validation and Discussion

The results of numerical simulations show that the numerical plan is well conducted and keeps a high rate of convergence. In this part, results for different cases are presented in order to show the validity of the model.

There is no exact solution for verification of the model accuracy beyond simple examples due to the complexity of the hydraulic fracturing problem. Geertsma and de Klerk (1969) presented an approximate solution for a two dimensional fracture with a Newtonian fluid. In this solution, the fracture length, fracture opening at the wellbore, and net pressure can be derived as:

$$L(t) = 2\left[\frac{16E\acute{q}_0^3}{21\pi^3\mu}\right]^{\frac{1}{6}} t^{\frac{2}{3}} = 2.0 \times 0.539\left[\frac{E\acute{q}_0^3}{\mu}\right]^{\frac{1}{6}} t^{\frac{2}{3}} \quad (16)$$

$$W_{well}(t) = \left[\frac{5376\mu q_0^3}{\pi^3 \acute{E}}\right]^{\frac{1}{6}} t^{\frac{1}{3}} = 2.36\left[\frac{\mu q_0^3}{\acute{E}}\right]^{\frac{1}{6}} t^{\frac{1}{3}} \quad (17)$$

$$\Delta p_w = \left[\frac{21}{16}\mu \acute{E}^2\right]^{\frac{1}{3}} t^{\frac{-1}{3}} = 1.09\left[\mu \acute{E}^2\right]^{\frac{1}{3}} t^{\frac{-1}{3}} \quad (18)$$

where $\acute{E}$ is plane-strain modulus of elasticity ($\acute{E}$ =2G/1- ν), and q_0 is the injection rate per unit height of the fracture ($q_0 = Q_0/h_f$). Geertsma's model usutilizes the assumption of smooth closing surfaces as the boundary condition at the fracture tip ($\partial w(L,t)/\partial x = 0$), which is in accordance with Barenblatt's model for cohesive cracks. Therefore, results are not necessarily similar to the results of the model with the zero pressure boundary condition at the tips. Geertsma also assumed that the flow rate is equal to the injection rate everywhere. The fluid storage in the fracture (as the width changes with time) is neglected in Geertsma's model. Since pressure in Geertsma's model is net pressure, no in situ stress was assumed in this model to make the comparison easier. The FE model indicates good agreement with the analytical solution for a 10 minute constant rate injection of a Newtonian fluid (Figures 15 and 16). The fracture length and net pressure results are in close agreement, while the FE model predicts a slightly higher width at later time than the Geertsma's model.

Figure 14 shows that the pressure decreases with time while the fracture length increases. This result is a consequence of assuming an infinite height for the fracture (KGD geometry), which implies that longer fractures require less pressure. In the KGD model, the net pressure gradient drops rapidly with fracture length and reaches an almost constant value.

The fracture mechanics solution of Rummel and Winter was used to calculate the stress intensity factor. In this approach, the peak pressure (P_C), is expressed as (Rummel and Winter, 1982):

Accepted manuscript doi:
10.1680/jencm.18.00018

$$P_C = \frac{1}{h_0+h_a}\left(\frac{K_{IC}}{\sqrt{R}} + S_H f + S_h g\right) \quad (19)$$

where S_h and S_H are minimum and maximum in-situ pressures, respectively. P_C is the critical hydraulic pressure and f, g and h, are dimensionless functions of stress intensity factors that are calculated from normalized crack length of a/r, r being diameter of the borehole and a crack length.

$$f(b) = -2\left[\frac{(b^2-1)}{\pi b^7}\right]^{0.5} \quad (20)$$

$$g(b) = (\pi b)^{0.5}\left(1 - \frac{2}{\pi}\sin^{-1}\frac{1}{b}\right) + 2(b^2+1)\left(\frac{b^2-1}{\pi b^7}\right)^{0.5} \quad (21)$$

$$h_0(b) = 1.3\frac{b-1}{1+b^{1.5}} + 7.8\frac{\sin\left[\frac{b-1}{2}\right]}{2b^{2.5}-1.7} \quad (22)$$

$$h_{a1} = (\pi b)^{0.5}\left(1 - \frac{2}{\pi}\sin^{-1}\frac{1}{b}\right) \quad (23)$$

In addition to the confining pressure, the injected fluid pressure is applied on borehole wall and fracture plane. Despite such complex stress conditions, stress intensity factor around the crack tip can be easily formulated using the superimposition principle of stress intensity factors.

$$K_I(P_m, P, P_a) = K_I(P_m) + K_I(P_m) + K_I(P) + K_I(P_a) \quad (24)$$

In the above equation, K_I specifies the stress intensity factor for mode I. P is the applied pressure and P_a which is expressed by P_a= P(x,0) determines the pressure distribution in fracture direction from x=(R,-R) to x=(R+a, R-a) (Dos Santos, et al. 2011).

The variations of stress intensity factor as a function of the crack length in the reservoir domain are shown in Figure 17. The results show a good agreement between the analytical and FEM results. Despite complex loading conditions and various loads in hydraulic fracturing, stress intensity field in the crack tips, created from any source of loading, can be formulated using the principle of superimposition of stress intensity factors.

9-Conclusion

Hydro-mechanical coupling is crucial to account for the effect of fluid injection on hydraulic fracture propagation. A loose coupling of hydraulic and mechanical processes was presented in this study. Loose coupling is somehow simple to implement like one-way coupling, but it holds promise for capturing much more of the complex nonlinear physics, thus is similar to a fully coupled method. The hydraulic fracturing has been investigated numerically through a FEM-based model in different stress intensity factors, J-Integral, elastic modulus, Poisson's ratio, fluid pressure and fluid viscosity. The model couples the fluid flow with fracture propagation while damage initiation and evaluation criteria have also been presented. The results show that Increasing stress intensity factor and J-Integral would increase crack propagation.

The variation of critical pressure of crack propagation according to crack length growth in

different pressures was studied. By increasing crack length, critical crack propagation pressure decreases. This shows that the bottom hole pressure drops with time while the fracture length increases. Mechanical properties of reservoir including elastic modulus and Poisson's ratio, would affect hydraulic fracturing directly. The results from the model suggest that increasing elastic modulus and Poisson's ratio of rock increases the crack propagation as the stress intensity factor also increases. Generally, increasing the fracturing fluid viscosity in injection operation can considerably increase the fracture stress intensity factor. In fact, higher fluid viscosity leads to increasing net wellbore pressure that acts on the fracture surface area, which results in further opening of the fracture. The results from this work can be applied in the analysis and optimization of hydraulic fracturing to avoid proppant bridging or job failure, especially where formation modulus contrast is a challenge such as fracturing in multi-layer reservoirs or shale formations.

Numerical simulations were carried out and the results were compared with analytical solutions. A high rate of convergence is observed which indicates the validity of the model. In the KGD model, the net pressure gradient drops rapidly with fracture length and reaches an almost constant value. The fracture mechanics solution of Rummel and Winter (1982) was used to calculate the stress intensity factor. The variation of stress intensity factor as a function of the crack length in the reservoir domain shows a good agreement between the analytical and FEM results.

Accepted manuscript doi:
10.1680/jencm.18.00018

Notation List

a	Crack length
$\mathbf{B}$	matrix, which transfers the net pressures into equivalent nodal forces
$\mathbf{H}$	to conclude the contributions of fluid leak-off and fluid injection
h_f	fracture height
E'	plane train modulus of elasticity
F	equivalent global nodal force of net pressure
K	stress intensity factor
$\mathbf{K}_{\mathrm{u}}$	global stiffness of solid elements
$\mathbf{K}_{\mathrm{w}}$	global flux stiffness of fluid elements
$\mathbf{L}$	global length stiffness of fluid elements
$L(t)$	fracture length changes with time
$\mathbf{L}'$	to determine the contribution of node displacements on fracture surface to fracture width
n	power law model parameter
$\mathbf{P}, \mathbf{P}_{\mathrm{n+1}}$	node net pressure and node net pressure at the n + 1-th step
Δp_{net}	pressure drop
q_0	injection rate per 1−ν unit height of the fracture
q_i	injection rate
S	collection of boundary conditions of flow
t	time
$\mathbf{U}_{\mathrm{i}}^{\mathrm{f}}(\mathrm{i}=\mathrm{n},\mathrm{n}+1)$	node displacement with contribution to fracture width at the i-th step
$\mathbf{U}$	global nodal displacement
u	component of velocity in x axis
v	component of velocity in y axis
v_x	average fluid velocity
w	fracture width
$\mathbf{W}$	a vector formed by the widths on of the nodes on fracture surface
$\mathbf{W}_{\mathrm{i}}(\mathrm{i}=\mathrm{n},\mathrm{n}+1)$	fracture width at the i-th step
$\mathrm{W}_{\mathrm{well}}(t)$	width of fracture
$\bar{w}$	height-averaged fracture width
w	component of velocity in z axis
Δx	length

Greek letters

δ_{p}	allowable testing function
σ	stress
ν	Poisson's ratio

μ	fluid viscosity

Accepted manuscript doi:
10.1680/jencm.18.00018

References

Adachi J., Siebrits E., Peirce A., and Desroches J., Computer simulation of hydraulic fractures, Int. J. Rock Mech. Min. Sci., 44, pp. 739–757, 2007.

Andrson, T.L., Fracture Mechanics: Fundamentals and Applications, second edition, CRC, 1994.

Barsom, John M. and Rolfe, Stanley T., Fracture and Fatigue Control in Structures: Application of Fracture Mechanics, Philadelphia, 1999.

Chen, Y. M. Numerical computation of dynamic stress intensity factors by a Lagrangian finite-difference method (the HEMP code). Engineering Fracture Mechanics, 7(4): 653- 660, 1975.

Crittendon, B.C., The mechanics of design and interpretation of hydraulic fracture treatments, Journal of Petroleum Technology, (October), pages: 21–9, 1959.

Dahi-Taleghani A. Analysis of hydraulic fracture propagation in fractured reservoirs: an improved model for the interaction between induced and natural fractures, PhD dissertation, Austin,Texas: The University of Texas at Austin; 2009.

Delorenzi HG, On the energy release rate and the J-integral for 3-D crack configurations, Int. J. Fract. 19, 183–193, 1982.

Devloo PRB et al. A finite element model for three dimensional hydraulic fracturing. Math Comput Simul; 73:142–55, 2006.

Dos Santos, J.S., T.P. Ballestero and E. Da Silva Pitombeira, An Analytical Model for Hydraulic Fracturing in Shallow Bedrock Formations, Ground Water, 49(3): 415-425, 2011.

Erdogan, F. and Sih, G.C. On the crack extension in plates under plane loading and transverse shear. Journal of Basic Engineering, 85:519-527, 1963.

F.K. Benra, H.J.Dohmen, J.pei, S.Schuster, B.Wan, A comparison of one- way and two-way coupling methods for numerical analysis of fluid structure interactions, Journal of applied mathematics, ID 853560, 2011.

Fredrich, J., Deitrick, G., Arguello, J., de Rouffignac, E., Reservoir compaction, surface subsidence, and casing damage: a geomechanics approach to mitigation and reservoir management. Proceeding of SPE/ISRM EUROCK 1998, No. 47284. SPE and ISRM, 1998.

H.K. Versteeg and W. Malalasekara, An Introduction to Computational Fluid Dynamics: The Finite Volume Method, Prentice-Hall, 1995.

J.Q. Bao , E. Fathi, S. Ameri, A coupled finite element method for the numerical simulation of hydraulic fracturing with a condensation technique, Engineering Fracture Mechanics 131, 269–281, 2014.

J.O. Wilkes, Fluid Mechanics for Chemical Engineers, Prentice Hall, 1999.

Harrison, E., Kieschnick, W.F., McGuire, W.J., The mechanics of fracture induction and extension, Petroleum Trans AIME, Vol. 201 pages: 252–63, 1954.

Hubbert, M.K., Willis, D.G., Mechanics of hydraulic fracturing, Journal of Petroleum Technology, 9(6), pages: 153–68, 1957.

Lewis, R., Sukirman, Y. Finite element modelling for simulating the surface subsidence above a compacting hydrocarbon reservoir. Int. J. Numer. Anal. Methods Geomech. 18, 619 – 639, 1993a.

Lewis, R., Sukirman, Y., Finite element modelling of three- phase flow in deforming saturated oil reservoirs. Int. J. Numer. Anal. Methods Geomech. 17, 577–598, 1993b.

Lewis, R., Ghafouri, H., A novel finite element double porosity model for multiphase flow through deformable fractured porous media. Int. J. Numer. Anal. Methods Geomech. 21, 789 – 816, 1997.

M.J. Economides and K.G. Nolte. Reservoir Simulation. John Wiley and Sons, LTD, 3, 9-3, 2000.

Nuismer, R., An energy release rate criterion for mixed mode fracture, International Journal of Fracture 11, pages 245-250, 1975.

O. K. Mahabadi; A. Lisjak; A. Munjiza; and G. Grasselli, New Combined Finite-Discrete Element Numerical Code for Geomechanical Applications, International Journal of Geomechanics, 12, 676-88, 2012.

Osorio, J., Chen, H., Teufel, L., Numerical simulation of the impact of flow-induced geomechanical response on the productivity of stress-sensitive reservoirs. Proceedings of the 15th Reservoir Simulation Symposium, No. 51929. SPE, Richardson, TX, pp. 373–387, 1999.

Rummel, F. and R.B. Winter, Application of laboratory fracture mechanics data to hydraulic fracturing field tests. 1st Japan-USA Symp on Fracture Mechanics Approach, Hydraulic Fracture and Geothermal Energy, Sendai, Japan. pp: 495-501 in Proc., 1982.

Settari, A., Mourits, F., Coupling of geomechanics and reservoir simulation models. In: Siriwardane, Zaman (Eds.), Computer Methods and Advances in Geomechanics. Balkema, Rotterdam, pp. 2151–2158, 1994.

Settari, A., Walters, D., Advances in coupled geomechanical and reservoir modeling with applications to reservoir compaction. Proceedings of the 15th Reservoir Simulation Symposium, No. 51927. SPE, Richardson, TX, pp. 345–357, 1999.

Shih, C. F. B. Moran, and T. Nakamura, Energy Release Rate Along a Three-Dimensional Crack Front in a Thermally Stressed Body, International Journal of Fracture, 30, pp 79-102, 1986

Sih, G.C, Strain energy density factor applied to mixed mode problems, International Journal of Fracture 10, 305-321, 1974.

T.K. Perkins and L.R. Kern, Widths of Hydraulic Fractures, Journal of Petroleum Technology, 9, 937–949, 1961.

Z.Yun, Y.Hui, Coupled fluid structure flutter analysis of a transonic fan, Chinese Journal of Aeronautics, vol.24, 258-264, 2011.

Accepted manuscript doi:
10.1680/jencm.18.00018

Figure captions

Figure 1: PKN fracture Geometry

Figure 2: KGD fracture Geometry

Figure 3: penny-shaped fracture Geometry

Figure 4: Fluid flowing laterally through a narrow fracture

Figure 5: Discretization with finite elements

Figure 6: Semi-elliptical fracture and horizntal borehole inside a shale reservoire

Figure7: System coupling in Workbench

Figure 8: Fracture inside borehole after coupling

Figure 9: Stress intensity factor vs Crack length

Figure 10: J-Integral vs Crack length

Figure 11: Pressure vs Crack length

Figure 12: Stress intensity factor vs Viscosity

Figure 13: Young's modulus vs Stress intensity factor

Figure 14: Poisson’s ratio vs Stress intensity factor

Figure 15: Variation of pressure with crack length

Figure 16: Variation of crack length with time

Figure 17: Variation of stress intensity factor with crack length

Accepted manuscript doi:
10.1680/jencm.18.00018

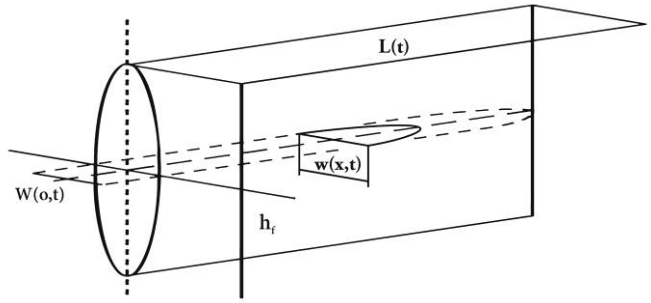

Figure 1

Accepted manuscript doi:
10.1680/jencm.18.00018

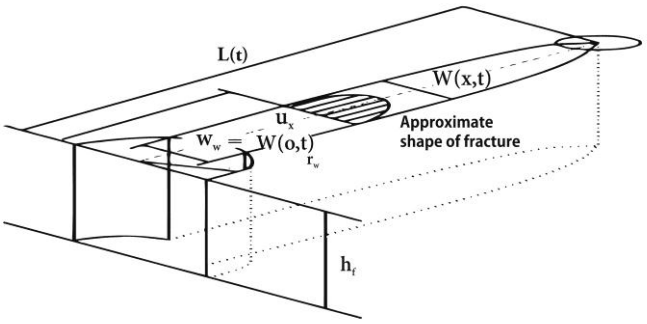

Figure 2

Accepted manuscript doi:
10.1680/jencm.18.00018

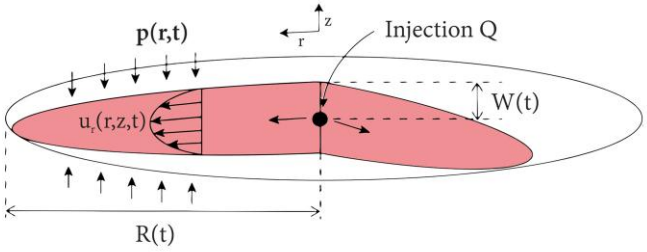

Figure 3

Accepted manuscript doi:
10.1680/jencm.18.00018

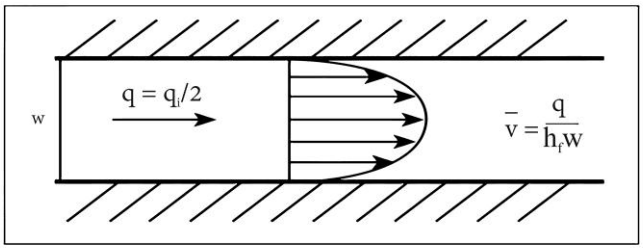

Figure 4

Accepted manuscript doi:
10.1680/jencm.18.00018

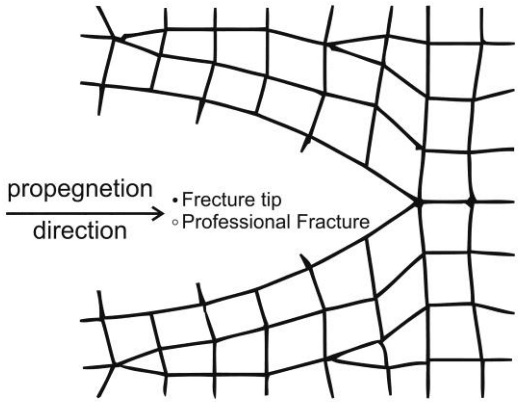

Figure 5

Accepted manuscript doi:
10.1680/jencm.18.00018

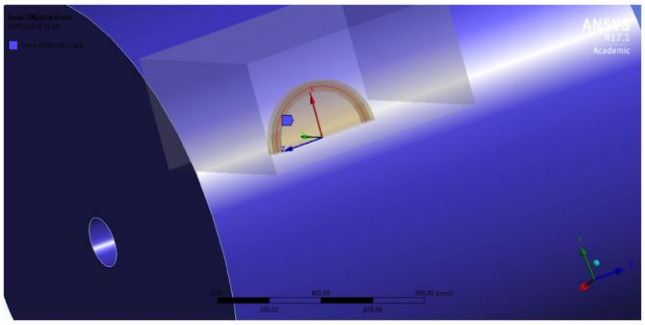

Figure 6

Accepted manuscript doi:
10.1680/jencm.18.00018

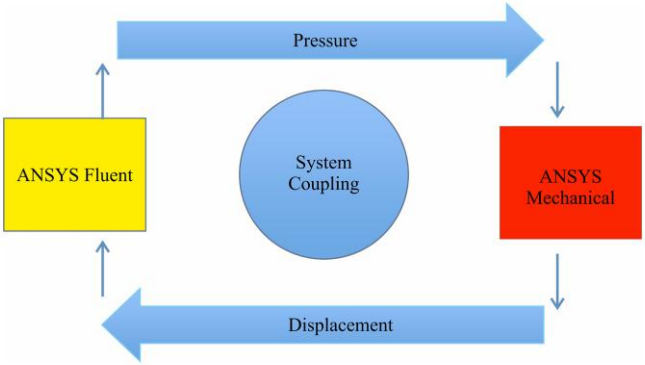

Figure 7

Accepted manuscript doi:
10.1680/jencm.18.00018

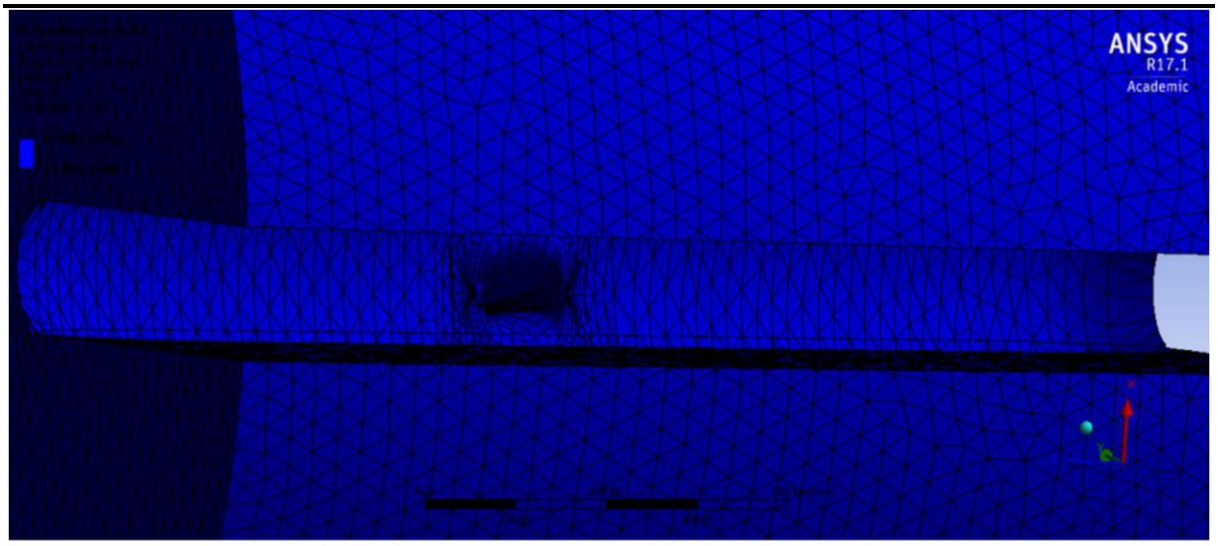

Figure 8

Accepted manuscript doi:
10.1680/jencm.18.00018

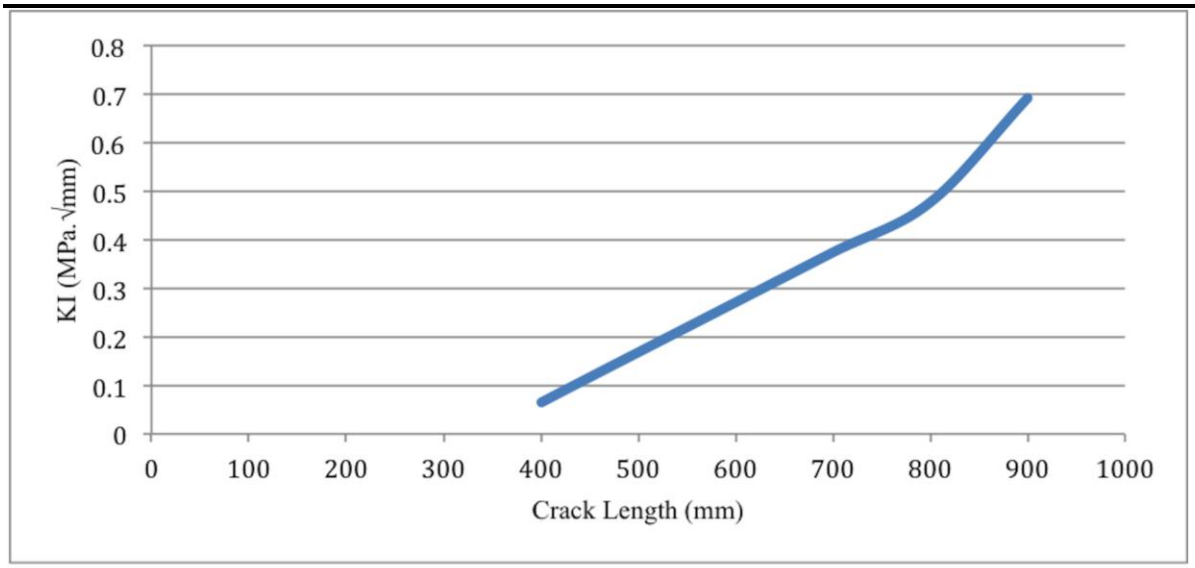

Figure 9

Accepted manuscript doi:
10.1680/jencm.18.00018

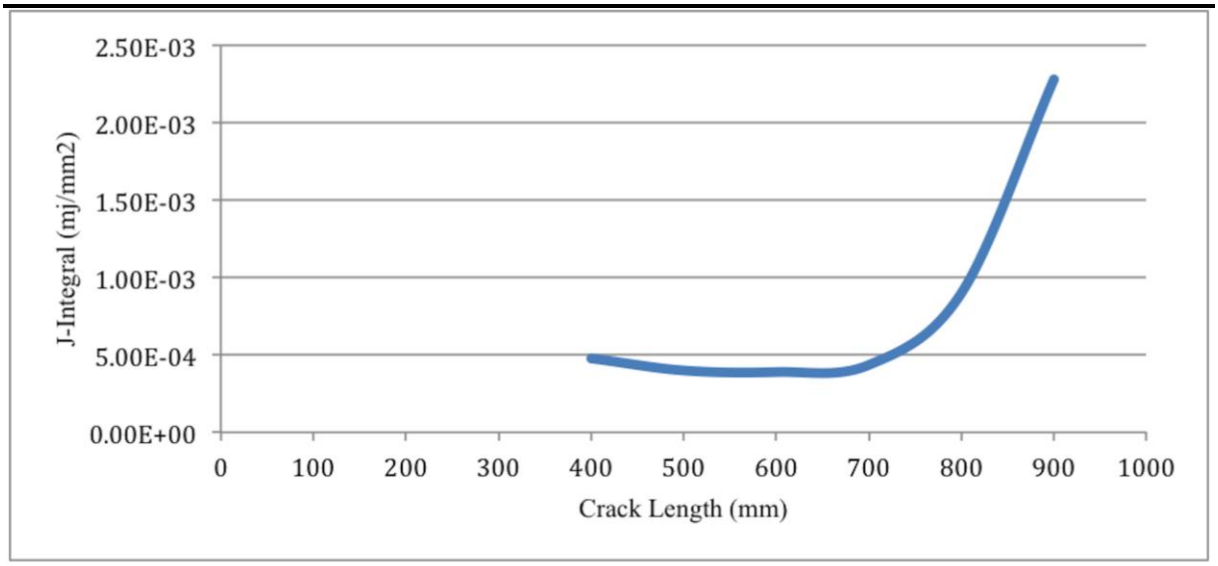

Figure 10

Accepted manuscript doi:
10.1680/jencm.18.00018

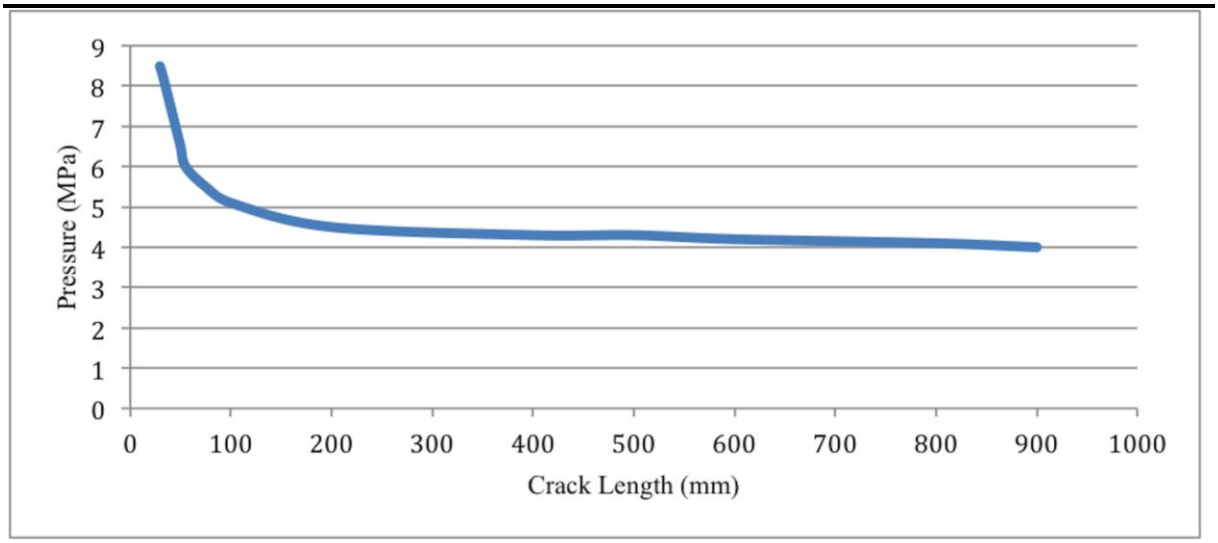

Figure 11

Accepted manuscript doi:
10.1680/jencm.18.00018

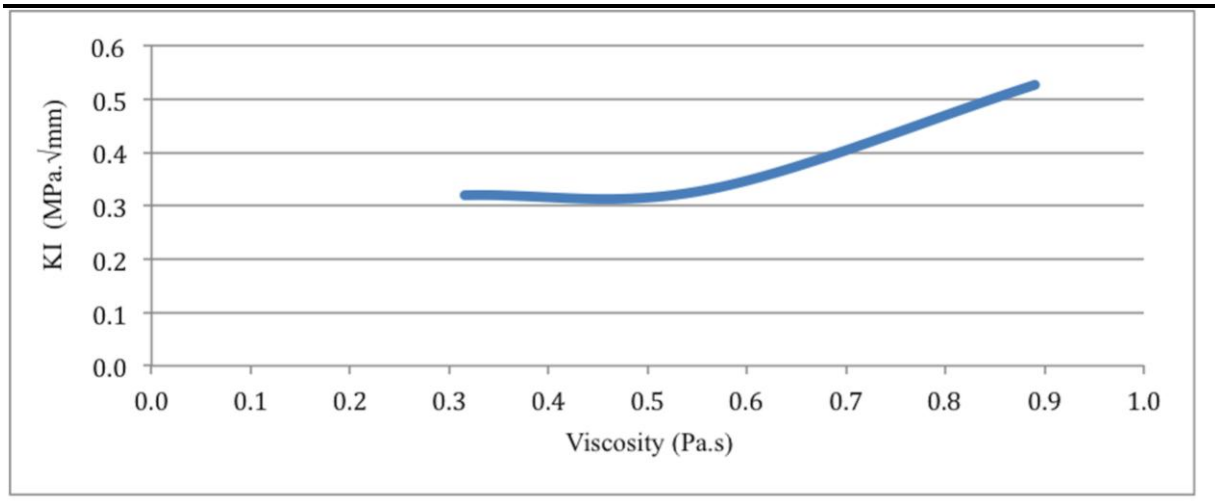

Figure 12

Accepted manuscript doi:
10.1680/jencm.18.00018

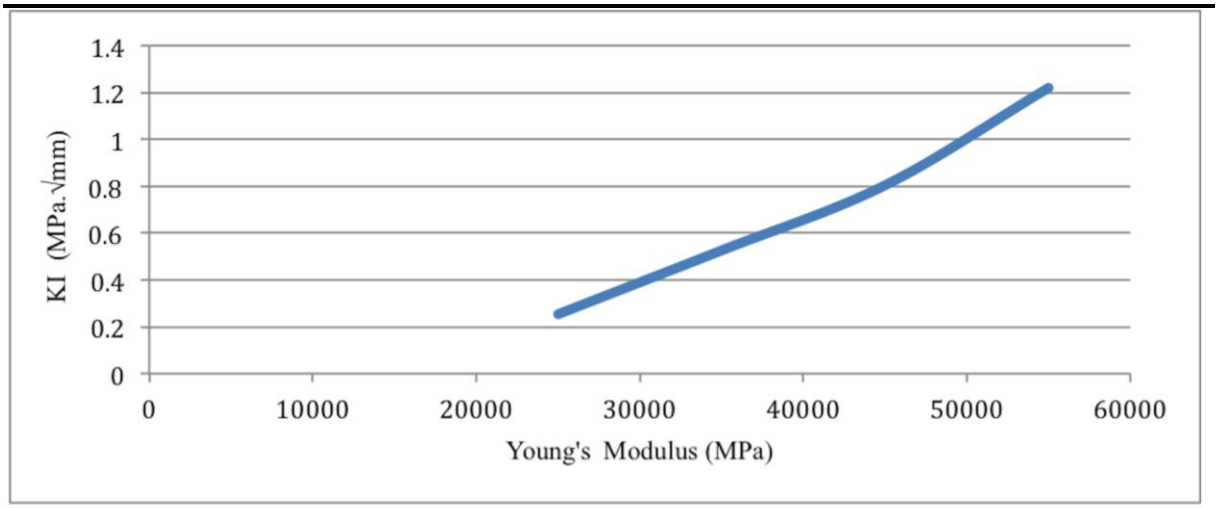

Figure 13

Accepted manuscript doi:
10.1680/jencm.18.00018

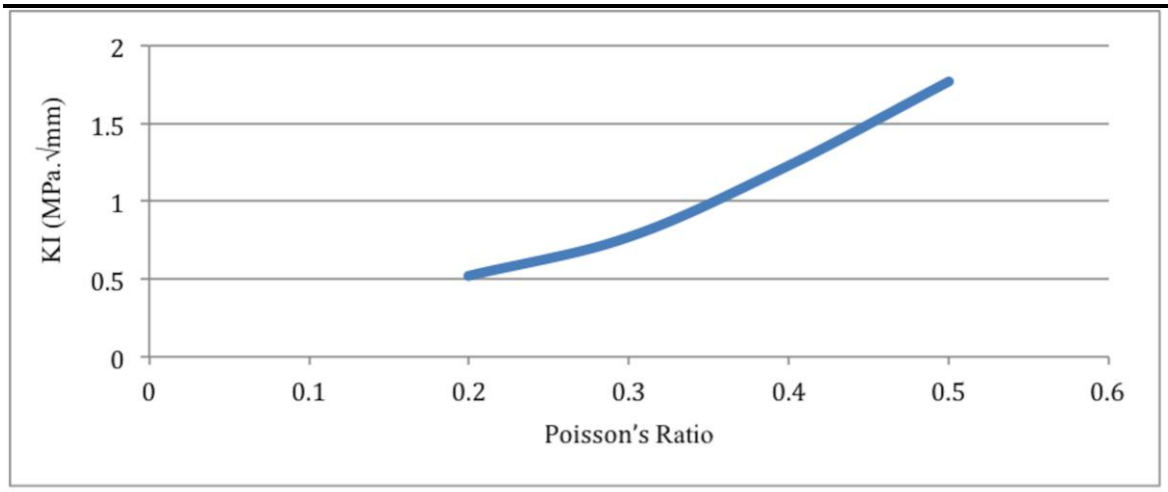

Figure 14

Accepted manuscript doi:
10.1680/jencm.18.00018

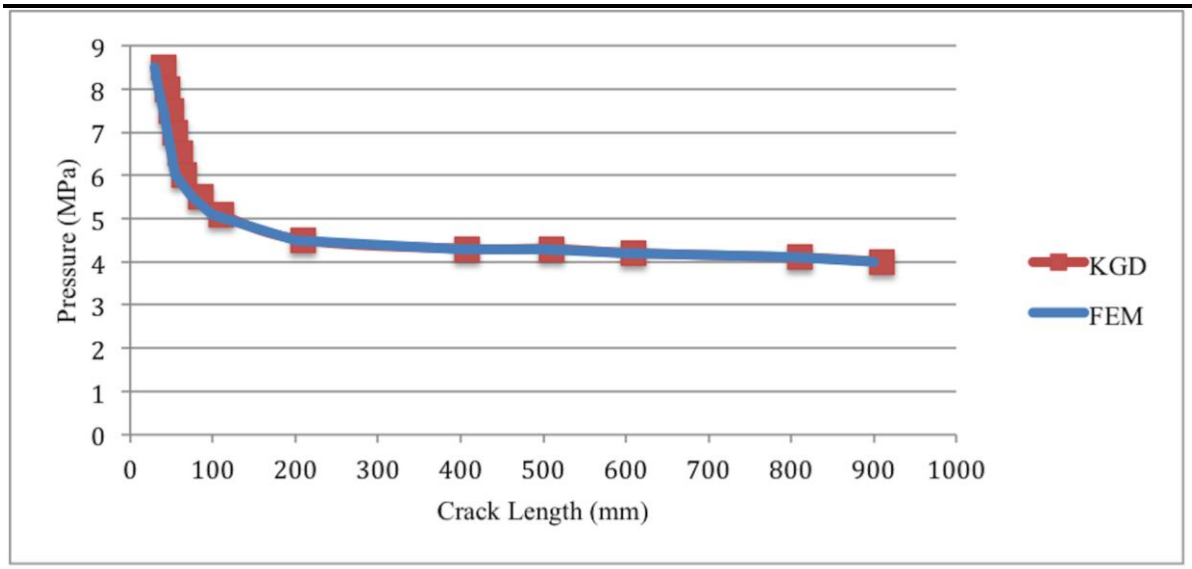

Figure 15

Accepted manuscript doi:
10.1680/jencm.18.00018

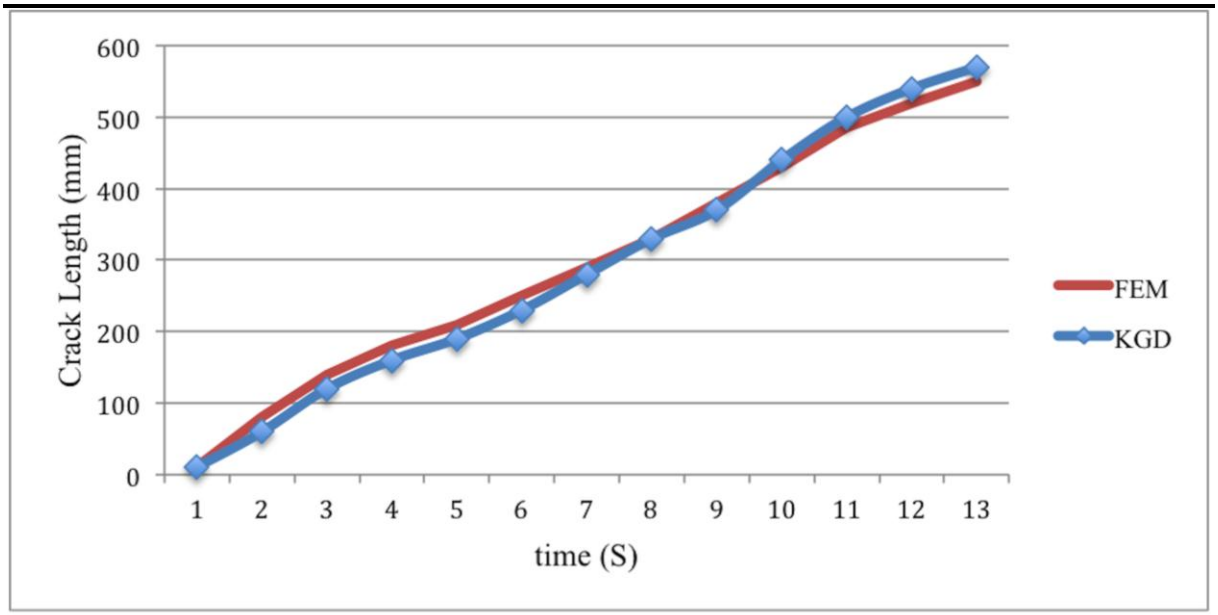

Figure 16

Accepted manuscript doi:
10.1680/jencm.18.00018

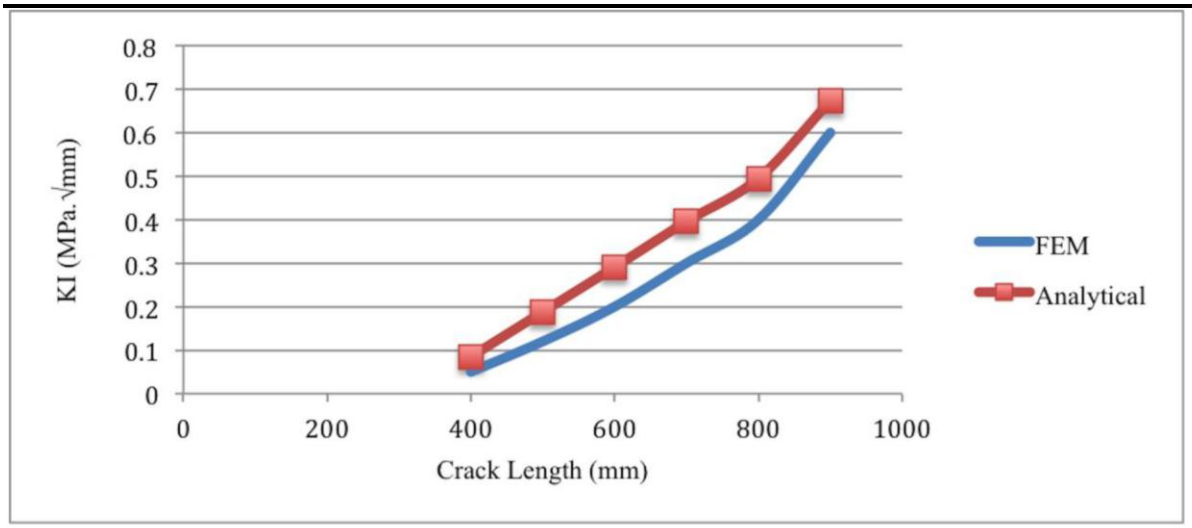

Figure 17